Universal Resonant Parameter Design Method Based on Multiple Boundary Constraints for Wireless Fast Charging

Yongbin Jiang, *Member, IEEE*, Yue Wu, *Student Member, IEEE*, Yaohua Li, *Student Member, IEEE,* Ning Wang, Xipei Yu, *Student Member, IEEE*, Xiaohua Wang, *Senior Member, IEEE*, and Yi Tang, *Senior Member, IEEE*

***Abstract*—Traditional resonant parameter design methods below MHz applications primarily rely on designer's experience and labor-intensive trial-and-error processes, which are not only time-consuming and inefficient but also fail to optimize system performance. This research proposes a universal resonant parameter design method based on multiple boundary constraints (MBCs) guiding engineers to complete the system design efficiently for wireless fast charging. This design method comprehensively considers multiple factors in parameter design and innovatively transforms them into constraint relationships, which are then mapped onto a two-dimensional plane graph to optimize the selection of self-inductances for the transmitting and receiving coils. Beyond rapidly generating an optimized coil design, this design method can also assist designers in refining unreasonable design specifications, significantly enhancing design efficiency and ensuring design results completely leverage superior system performance. According to experimental results, the coils developed with MBCs-based method not only enable WPT system to obtain outstanding steady-state and dynamic performance, but also result in high transfer efficiency. With a coupling coefficient *k* of 0.183 or 0.151, the maximum transfer efficiency can achieve 94.83% or 93.93% under the power rating of 1kW as well as 91.25% or 87.87% under the power rating of 288W (light load condition).**

***Index Terms*—Fast charging, multiple boundary constraints (MBCs), parameter design, wireless power transfer.**

I. Introduction

Wireless power transfer (WPT) technology has emerged as a groundbreaking solution for efficiently transmitting electrical energy without physical connectors, opening doors to new possibilities across various fields. From medical implants [1], [2], to consumer electronics [3], [4], drones [5], underwater robots [6], [7], industrial automation [8], [9], and electric vehicles [10], [11], [12], ranging from several watts to tens of kilowatts, the widespread applications of WPT technology can significantly improve convenience, enhance user experience, and extend the device longevity. Especially since Tesla's high-profile launch of the Robotaxi [13], WPT technology has once again sparked a wave of interest in academic and commercial circles worldwide.

Obviously, it is crucial to reasonably and efficiently design a WPT system for various application scenarios to achieve fast, stable, and safe battery charging with a high transfer efficiency. As the most critical energy conversion module in a WPT system, the resonant network has a decisive impact on the key performance of the WPT system [14]. Before designing a specific resonant network, it is essential to optimize its resonant parameters based on multiple design criteria and requirements.

Many researchers are dedicated to developing practical methods for designing resonant network parameters. In [15], the authors take the design of a 500W wireless charging system for a city car as an example, using a combination of experience and simulation to select the resonant parameters, but without achieving an optimized design. In [16], a practical design process of resonant parameters of the WPT system is presented by considering multiple factors including current rating, output dc voltage, and transfer power under misalignments. However, they don't provide an intuitive and universal design methodology. In [17], a multi-objective optimization method of a double-D pad for a WPT system is proposed based on the WPT2 defined by SAE J2954 [18]. However, the method for designing coils mentioned above is not universally applicable, as there are only a few specific applications where resonant parameters have established selection standards. In order to meet the constant current (CC) and constant voltage (CV) charging of batteries, the authors are dedicated to developing and deriving a series of WPT systems capable of providing CC and CV output. Unfortunately, the authors cannot provide a resonant network parameter design solution [19]. In summary, there is a lack of a universal method for resonant network parameter design that comprehensively considers multiple factors.

With the continuous development of battery technology, many application demands have an urgent need for shorter charging times, thus requiring WPT technology to enable fast charging. Traditional wireless charging methods for batteries typically employ charging profiles that maintain a CC stage and a CV stage [20], [21], [22]. Since the battery voltage is relatively low at the beginning of CC stage, the charging power starts at a minimum level, slowly rising to its peak near the end of the CC stage, which ultimately results in a slower overall charging rate. Intuitively, applying a higher charging current during the CC charging stage can increase charging rate, but it also places greater demands on thermal management design and accelerates battery aging [23], [24], [25]. Therefore, by incorporating constant power (CP) charging to replace part of

This work is supported by XXX

the CC stage, the wireless charger can either increase the charging speed with the same setup or reduce overall size and cooling material costs, which eliminates the need for excessive thermal design, as well as mitigates the issue of battery aging.

The typical three-stage charging process for the battery is shown in Fig. 1. In CC stage, the WPT system first charges the battery with the maximum charging current $I_{2\max}$. As the charging process goes, it will switch from CC stage to CP stage when the charging power reaches the highest charging power $P_{2\max}$. When the charging voltage V_2 reaches its maximum value $V_{2\max}$, it will switch from CP stage to CV stage. In CV stage, the highest charging voltage $V_{2\max}$ is applied to charge the battery until the charging process is completed. Based on the four special operating points A, B, C, and D shown in Fig. 1, the relationships between the battery voltage, current, power, and equivalent dc resistance at four charging time points are

$$\begin{cases} V_{2A} < V_{2B} < V_{2C} = V_{2D} \\ I_{2A} = I_{2B} > I_{2C} > I_{2D} \\ P_{2A} < P_{2B} = P_{2C} > P_{2D} \\ R_{LA} < R_{LB} < R_{LC} < R_{LD} \end{cases} \tag{1}$$

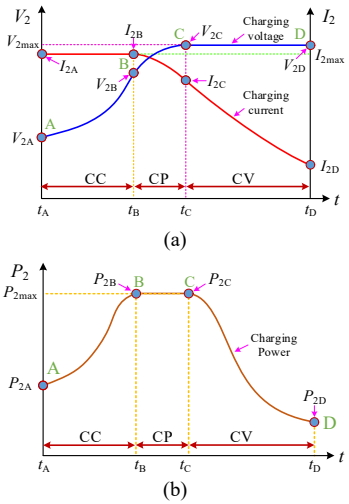

Fig. 1. Charging curves of three-stage charging mode for batteries. (a) Charging voltage V_2 and charging current I_2 versus charging time. (b) Charging power P_2 versus charging time.

With the continuous development of fast charging technology for batteries, the charging power is constantly increasing, which raises higher design requirements for WPT systems. Therefore, it is urgent to develop a universal resonant parameter design method that can adapt to multi-scenario applications and achieve fast, stable, safe, economical, and efficient charging. As shown in Fig. 2, when performing the specific design of resonant parameters, an effective parameter design method must take into account multiple factors, including the transfer characteristics of the resonant network, system control strategies, battery charging methods, misalignments of the transmitting (Tx) and receiving (Rx) coils, the voltage and current stresses on resonant components, charging efficiency, and other related indicators or requirements. The structural design of resonant coils can only be carried out after obtaining optimized resonant parameters that meet all electrical characteristics. Moreover, when a resonant parameter design method is proposed, how can the quality of this method be evaluated? Fig. 2 presents four basic evaluation metrics that can roughly assess the quality of a parameter design method, which include:

1) Universality: it can be effectively used in various applications and conditions;
2) Adaptability: it can be adjusted to different application environments, handling various constraints and objectives;
3) Ease of Use: it is simple to operate and provides clear guidance to designers, reducing development time and learning costs;
4) Efficiency and Effectiveness: it should be able to quickly generate solutions that meet the design requirements and deliver high performance, stability, and other key metrics.

In addition to the four basic metrics mentioned above, a more advanced and intelligent design method should be capable of assisting designers in reasonably adjusting the relevant design requirements to optimize the overall performance of the WPT system, which is crucial in practical engineering applications.

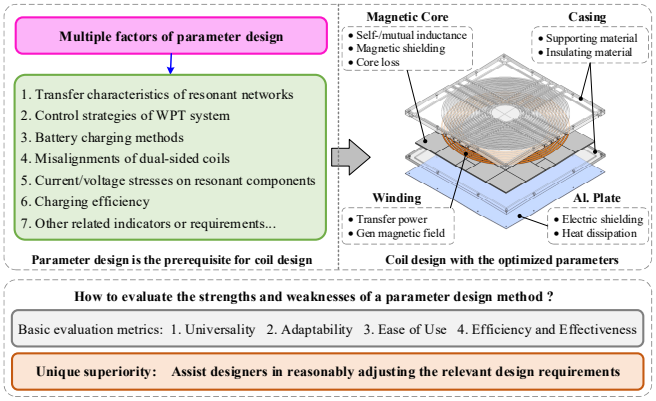

Fig. 2. Design of resonant network parameters and evaluation of design methods.

To highlight the innovative contribution of this paper, Fig. 3 compares the traditional WPT system design method based on coil design objectives with the proposed approach based on multiple boundary constraints (MBCs). As shown in Fig. 3(a), conventional methods usually begin by setting one or more objectives for the Tx and Rx coils, such as quality factor [26], [27], transfer efficiency & power density [28], transfer efficiency & material cost & misalignment [29], coupling coefficient and leakage flux [17], and so on. Based on the structural and positional constraints, coils are designed and fabricated, which are experimentally measured to obtain their self- and mutual inductances, and subsequently used to construct the WPT system. However, validating whether the system with designed coils meets various performance requirements is a complex and time-consuming process. If any of these requirements are not met, the coils must be redesigned and refabricated, which introduces significant cost and design inefficiencies. Moreover, traditional methods provide limited guidance on how to adjust coil parameters effectively once design issues are identified.

To overcome the shortcomings of the traditional design method of the WPT system that prioritizes coil design

objectives, Fig. 3(b) presents a universal resonant parameter design method of the WPT system based on MBCs. Rather than relying solely on predefined coil objectives, this method first assumes a reasonable range for the coupling coefficient based on structural and positional parameters of two coils. It then comprehensively incorporates various design considerations into unified MBCs. Moreover, a two-dimensional plane graph is introduced to guide the selection of coil self-inductances within the feasible region defined by MBCs. Finally, the coil design is then performed within these boundaries, and feasibility verification is simplified to confirming that the actual coupling falls within the assumed range. Compared to traditional methods, this approach inherently embeds important, complex, and time-consuming validation processes into the design stage with the MBCs and are reflected in the allowable ranges of self-inductance values for the Tx and Rx coils. In addition to producing the optimized coil design, this MBCs-based design method can also assist designers revising unreasonable indicators, significantly boosting design efficiency and ensuring the design results completely leverage superior system performance.

The remainder of this article is organized as follows. Section II presents the basic analysis of the WPT system and introduces the leap frequency phase shift control (LFPSC) strategy. Section III presents the derivation process of MBCs for optimizing the resonant parameters. Section IV introduces a case-study to detail the lprocess of designing a resonant network using MBCs. Section V validates the design results through simulated and experimental testing. Finally, Section VI concludes this article.

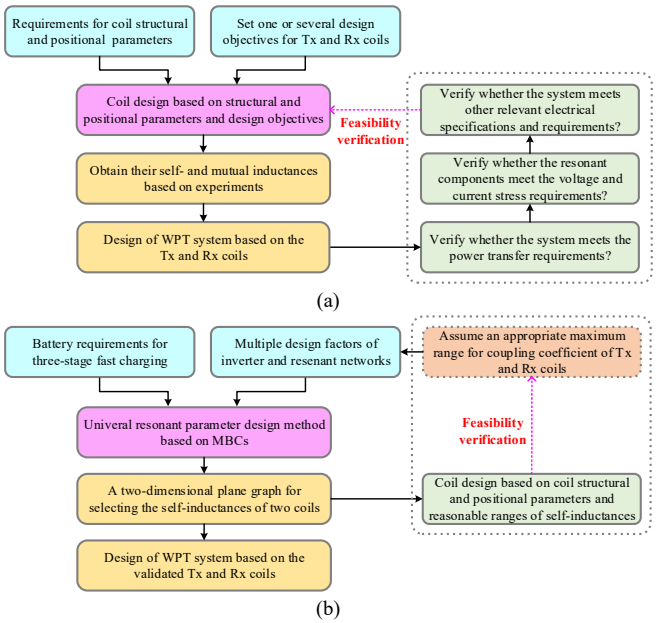

Fig. 3. Comparison of design methods of the WPT system. (a) Traditional design methods based on coil design objectives. (b) Proposed design method based on MBCs.

II. Basic Analysis of the WPT System

A. Fundamentals of the WPT System

The schematic of the SS-type WPT system is shown in Fig. 4. Its configuration comprises a high-frequency full-bridge inverter, an SS-type resonant network and a full-bridge rectifier. The inverter operates in the complementary mode at the frequency ω_s that ranges from tens of kHz to hundreds of kHz. It converts a dc voltage V_1 into a high-frequency ac square voltage v_{ab} that stimulates the primary resonant coil L_1 and resonant capacitor C_1. Subsequently, the high-frequency alternating magnetic field is generated by L_1, inducing a high-frequency ac voltage in the secondary resonant coil L_2, which powers a load R_L with a rectifier.

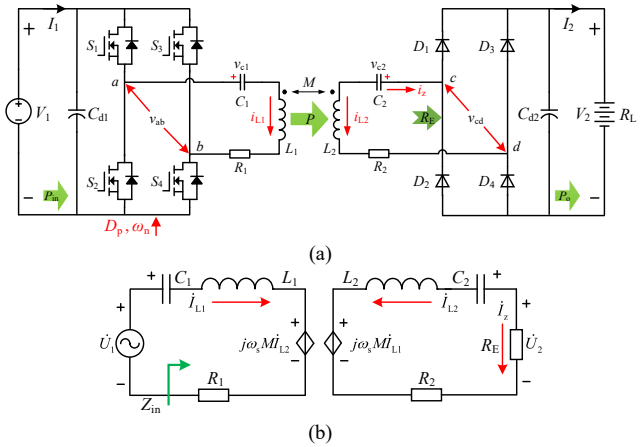

Fig. 4. (a) Schematic of an SS-type WPT system. (b) Its ac equivalent circuit.

In general, the fundamental harmonic analysis is commonly applied in the WPT system [30] and its ac equivalent circuit is shown in Fig. 4(b). U_1 and U_2 represent the root mean square (rms) values of fundamental components of v_{ab} and v_{cd}, respectively. I_{L1} and I_{L2} represent the rms values of Tx and Rx resonant currents, respectively. R_1 and R_2 denote the equivalent series resistors (ESRs) of the resonant network. L_1 and L_2 represent the self-inductances of Tx and Rx coils, respectively. M is their mutual inductance and their coupling coefficient, k, satisfies

$$k = \frac{M}{\sqrt{L_1 \times L_2}} \tag{2}$$

For simplicity, the Tx and Rx resonant frequencies are set to be equal to ω_0 that satisfies

$$\omega_0 = \frac{1}{\sqrt{L_1 C_1}} = \frac{1}{\sqrt{L_2 C_2}} \tag{3}$$

Therefore, the per-unit value of the operating frequency ω_n can be defined as

$$\omega_n = \omega_s / \omega_0 \tag{4}$$

where ω_s is the actual operating frequency of the inverter.

B. Characteristics of Resonant Network

To achieve fast and stable charging of the battery, it is essential to fully leverage the transfer characteristics of the resonant network. Based on Fig. 4(b) and Eq. (1) in [27], when R_1 and R_2 are neglected, the trans-conductance gain of the resonant network, G_{ivss}, can be obtained by

$$G_{ivss} = \left|\frac{\dot{I}_Z}{\dot{U}_1}\right| = \frac{kL_2\omega_n^3}{\sqrt{L_1L_2(R_E^2\omega_n^2(\omega_n^2-1)^2 + \omega_0^2L_2^2(-1+2\omega_n^2+(-1+k^2)\omega_n^4)^2)}} \tag{5}$$

According to (5), G_{ivss} is a function of the ac equivalent load resistance R_E and ω_n. As shown in Fig. 5(a), when the WPT system operates at point M, it will exhibit constant current characteristics regardless of load variations, which is crucial for CC charging of battery. When ω_n=1, G_{ivss} can be obtained by

$$G_{ivss}(\omega_n = 1) = \frac{1}{k\omega_0\sqrt{L_1 L_2}} \tag{6}$$

According to (5), the voltage gain of the resonant network, G_{vss}, can also be obtained by

$$\begin{aligned} G_{vss} &= \left|\frac{\dot{U}_2}{\dot{U}_1}\right| = G_{ivss} \times R_E \\ &= \frac{kL_2\omega_n^3 R_E}{\sqrt{L_1 L_2 (R_E^2\omega_n^2(\omega_n^2-1)^2 + \omega_0^2 L_2^2(-1+2\omega_n^2+(-1+k^2)\omega_n^4)^2)}} \end{aligned} \tag{7}$$

Similarly, according to (7), G_{vss} is also a function of R_E and ω_n. When the system operates at point N_L or N_H in Fig. 5(b), it will exhibit constant voltage characteristics regardless of load variations, which is crucial for CV charging of battery. Based on [31], the operating frequencies at N_L and N_H are

$$\begin{cases} \omega_{nL} = 1/\sqrt{1+k} & \cdots \text{ Point } N_L \\ \omega_{nH} = 1/\sqrt{1-k} & \cdots \text{ Point } N_H \end{cases} \tag{8}$$

Substituting (8) into (7) respectively, it can be obtained that

$$G_{vss}(\omega_{nL}) = G_{vss}(\omega_{nH}) = \sqrt{L_2/L_1} \tag{9}$$

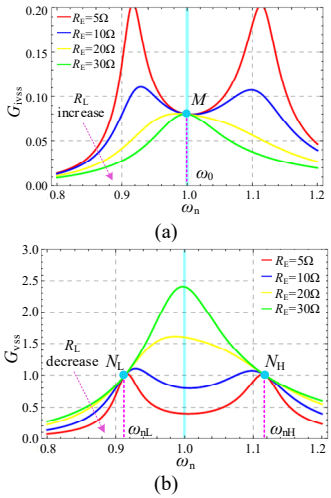

Fig. 5. Transfer characteristics of the ideal SS-type resonant network, when L_1=L_2=116.86uH, C_1=C_2=30nF and k=0.2. (a) G_{ivss} versus ω_n with different R_E. (b) G_{vss} versus ω_n with different R_E.

C. Leap-Frequency Phase Shift Control

To fully utilize the CC/CV characteristics of the resonant network shown in Fig. 5, a leap frequency phase shift control (LFPSC) strategy is adopted to achieve the three-stage fast charging of the battery, which is depicted in Fig. 6. According to the analysis results in Section II.B, when ω_n = 1, the WPT system will exhibit CC characteristics regardless of load variations. Correspondingly, when ω_n = ω_{nL} or ω_{nH}, the WPT system will exhibit CV characteristics regardless of load variations. Fully utilizing these characteristics can significantly enhance the stability of the WPT system [32].

Based on Fig. 6, the charging process starts by calculating the equivalent dc resistance of the battery R_L based on the secondary controller sampled signals (charging voltage V_2 and current I_2). By comparing the calculated value R_L with the preset critical resistances R_{LB} and R_{LC} in (1), the charging mode will be decided. When the battery is charged at CC stage (or CP stage), the inverter will operate at the constant frequency phase-shift control with ω_n=1 and set the reference signal of CC command (or CP command) to I_{2ref} (or P_{2ref}). When the battery operates at CV stage, the inverter will operate at the constant frequency phase-shift control with $\omega_n = 1/\sqrt{1-k}$ and set the reference signal of CV command to V_{2ref}.

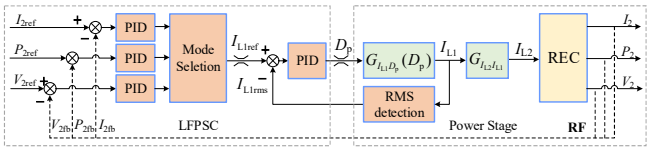

Fig. 6. Flow chart of LFPSC strategy based on the equivalent load resistor.

D. Minimum Phase-Shift Duty Cycle

As shown in Fig. 1(b), the charging power undergoes large variations throughout the entire three-stage charging process. When the LFPSC strategy is adopted in Fig. 6, the control variable phase-shift duty cycle, D_p, will inevitably undergo significant variations. However, a smaller D_p will adversely affect the performance of the WPT system. Take the CC charging stage as an example. To achieve the CC charging characteristic of the SS-type WPT system, the inverter should operate at the resonant frequency. The typical operating waveforms of the WPT system with LFPSC in CC stage are shown in Fig. 7.

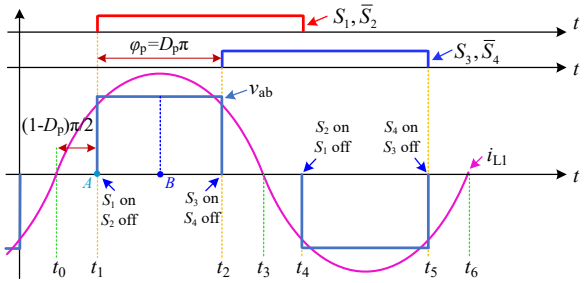

Fig. 7. Operating waveforms of the WPT system with LFPSC in CC stage.

On the one hand, when the inverter operates at Point M in Fig. 5(a) (i.e. ω_n=1), S_1 and S_2 of the inverter cannot achieve ZVS as long as D_p<1, resulting in a certain level of switching losses. Meanwhile, if i_{L1} remains constant, the switching losses increases as D_p decreases. Therefore, to minimize the switching losses of the inverter as much as possible during the whole charging process, the resonant network parameters should be designed to ensure that D_p does not become too small, thereby reducing the switching losses of the inverter to the greatest extent possible.

On the other hand, an excessively small D_p tends to introduce a large number of harmonics into the resonant network, thereby increasing the voltage and current stresses on resonant components [33]. In Fig. 7, the fundamental harmonic of the ac

square voltage v_{ab}, U_1, can be changed by adjusting the phase-shift duty cycle D_p, which can be calculated by [34]

$$U_1(D_p)=\frac{2\sqrt{2}}{\pi}V_1\sin[\frac{D_p\pi}{2}] \tag{10}$$

Moreover, based on (10), the total harmonics distortion (THD) of the output ac square voltage of the inverter versus D_p can be calculated by

$$\mathrm{THD}(D_p)=\frac{\sqrt{2\cos[D_p\pi]+0.5D_p\pi^2-2}}{2\sin[0.5D_p\pi]}\times 100\% \tag{11}$$

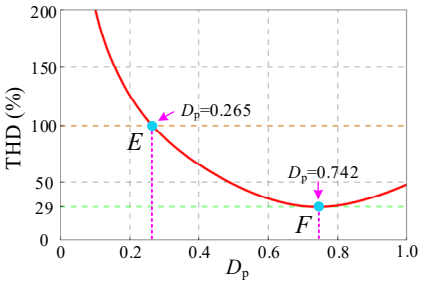

Fig. 8. Relationship between THD and D_p when the LFPSC is applied.

Based on (11), the relationship between THD and D_p is plotted in Fig. 8. Obviously, the smaller D_p (lower than 0.742) will lead to the larger THD of the output ac square voltage of the inverter. Therefore, D_p should be larger than a minimum value D_{pmin} in the whole charging process. Notably, assuming the maximum value of THD is set to 1, the corresponding D_{pmin} can be calculated as 0.265.

III. Multiple Boundary Constraints for Resonant Parameter Design

Before designing coils for practical applications, the first step is to determine the self-inductances of Tx and Rx coils. However, it requires a comprehensive consideration of multiple factors, including the transfer characteristics of the resonant network, system control strategies, fast charging (three-stage charging) methods, variations of coupling coefficient, the voltage and current stresses on resonant components and the limitation of minimum phase-shift duty cycle. Through detailed derivations, these multiple factors can be converted into multiple inequalities that constrain the self-inductances of Tx and Rx coils. The upper and lower limits of these inequalities will define the boundary values for the parameter optimization design of the self-inductances of Tx and Rx coils.

A. Summary of Design Requirements

According to the previous analysis, the design requirements of resonant parameters should satisfy:

1) Output Design Requirements

The output design requirements will be discussed in three stages: CC stage, CP stage, and CV stage.

In CC stage, ω_n is set to 1. When $D_p = 1$, the output dc current I_2 of the WPT system should be greater than the required maximum charging current I_{2max}. Meanwhile, to limit the minimum D_p, I_2 should be less than I_{2max} when $D_p = D_{pmin}$.

In CP stage, ω_n is set to 1. When $D_p = 1$, the output dc power P_2 of the WPT system should be greater than the required maximum charging power P_{2max}. Meanwhile, to limit the minimum D_p, P_2 should be less than P_{2max} when $D_p = D_{pmin}$.

In CV stage, ω_n is set to ω_{nH}. When $D_p = 1$, the output dc voltage V_2 of the WPT system should be greater than the required maximum charging voltage V_{2max}. Meanwhile, to limit the minimum D_p, V_2 should be less than V_{2max} when $D_p = D_{pmin}$.

These three aforementioned requirements are collectively referred to as the output design requirements.

2) Current Requirements of Coils

To ensure the safe operation of resonant coils during the whole charging process, the steady-state rms values of resonant coils currents on both sides should be less than the preset safety currents I_{L1safe} and I_{L2safe} respectively.

3) Voltage Requirements of Capacitors

To ensure the safe operation of resonant capacitors during the whole charging process, the steady-state rms values of resonant capacitor voltages on both sides should be less than the preset safety voltages V_{C1safe} and V_{C2safe} respectively.

B. Boundary Constraints for Output Design Requirements

1) Output Design Requirements in CC Stage

In CC stage, the equivalent dc resistance of the battery, R_L, gradually increases from R_{LA} to R_{LB}. According to (6) and (10), when ω_n=1, the trans-conductance gain of the system, G_{ivsys}, can be obtained with

$$G_{ivsys}(\omega_n=1,D_p)=\frac{8}{\pi^2\omega_0 k\sqrt{L_1L_2}}\sin[\frac{D_p\pi}{2}] \tag{12}$$

Based on (12), it is evident that G_{ivsys} is a monotonically increasing function of D_p and a monotonically decreasing function of k. In CC stage, the desired trans-conductance gain of the system is defined as K_{cc} (=I_{2max}/V_1). Hence, to meet the CC charging requirement when D_p=1, G_{ivsys} needs to be not less than K_{cc}, which is

$$G_{ivsys}(\omega_n=1,D_p=1)\ge K_{cc} \tag{13}$$

In addition, an excessively large G_{ivsys} will result in too small D_p. Therefore, to limit the minimum D_p, when D_p=D_{pmin}, it is required that G_{ivsys} should not exceed K_{cc}, which is

$$G_{ivsys}(\omega_n=1,D_p=D_{pmin})\le K_{cc} \tag{14}$$

By substituting (12) into (13) and (14), the self-inductances of Tx and Rx coils in CC stage should satisfy

$$\frac{64}{\pi^4\omega_0^2k^2K_{cc}^2L_1}\sin^2\left(\frac{D_{pmin}\pi}{2}\right)\le L_2\le\frac{64}{\pi^4\omega_0^2k^2K_{cc}^2L_1} \tag{15}$$

Given that the range of k is [k_{min}, k_{max}] and denoting the upper and lower limits of L_2 as L_{2ccu} and L_{2ccd} respectively, it can be determined that the range of L_2 is

$$\begin{cases}L_{2ccd}=\dfrac{64}{\pi^4\omega_0^2k_{min}^2K_{cc}^2L_1}\sin^2\left(\dfrac{D_{p\,min}\pi}{2}\right)\le L_2\\ L_{2ccu}=\dfrac{64}{\pi^4\omega_0^2k_{max}^2K_{cc}^2L_1}\ge L_2\end{cases} \tag{16}$$

2) Output Design Requirements in CP Stage

In CP stage, R_L gradually increases from R_{LB} to R_{LC}. Still setting ω_n=1, and based on (12), the output power P_2 is

$$P_2(\omega_n=1, D_p)=\frac{64V_1^2R_L}{\pi^4\omega_0^2k^2L_1L_2}\sin^2\left(\frac{D_p\pi}{2}\right) \tag{17}$$

Similar to CC stage, based on (17), P_2 is also a monotonically increasing function of D_p and a monotonically decreasing function of k. By considering both the maximum output power P_{2max} and the minimum D_p, P_2 should satisfy

$$\begin{cases} P_2(\omega_n=1, D_p=1)\ge P_{2max} \\ P_2(\omega_n=1, D_p=D_{pmin})\le P_{2max} \end{cases} \tag{18}$$

By substituting (17) into (18), the self-inductances of Tx and Rx coils in CP stage can be obtained. Moreover, considering that the range of k is [k_{min}, k_{max}] and the range of R_L is [R_{LB}, R_{LC}], with the upper and lower limits of L_2 denoted as L_{2cpu} and L_{2cpd} respectively, L_2 should satisfy

$$\begin{cases} L_{2cpd}=\dfrac{64V_1^2R_{LC}}{\pi^4\omega_0^2k_{min}^2L_1P_{2max}}\sin^2\left(\dfrac{D_{pmin}\pi}{2}\right)\le L_2 \\ L_{2cpu}=\dfrac{64V_1^2R_{LB}}{\pi^4\omega_0^2k_{max}^2L_1P_{2max}}\ge L_2 \end{cases} \tag{19}$$

By comparing (16) and (19) with the limits set for L_2 in CC and CP stages, it can be inferred that

$$\begin{cases} L_{2cpu}=\dfrac{64V_1^2R_{LB}}{\pi^4\omega_0^2k_{max}^2L_1P_{2max}}=\dfrac{64}{\pi^4\omega_0^2k_{max}^2L_1}\dfrac{V_1^2R_{LB}}{I_{2max}^2R_{LB}}=L_{2ccu} \\ L_{2cpd}=\dfrac{64V_1^2R_{LC}}{\pi^4\omega_0^2k_{min}^2L_1P_{2max}}\sin^2\left(\dfrac{D_{pmin}\pi}{2}\right)=\dfrac{R_{LC}}{R_{LB}}L_{2ccd}>L_{2ccd} \end{cases} \tag{20}$$

Then, the range of L_2 constrained in the CC and CP stages is not mutually independent. It is worth mentioning that to make (19) have a solution, it needs to satisfy

$$\sin^2\left[\frac{D_{pmin}\pi}{2}\right]<\frac{R_{LB}k_{min}^2}{R_{LC}k_{max}^2} \tag{21}$$

It is evident that when setting parameter design indicators, these indicators must satisfy (21); otherwise, there will be no solution.

3) Output Design Requirements in CV Stage

In CV stage, R_L increases from R_{LC} to R_{LD}. The resonant network exhibits constant voltage characteristics when ω_n=ω_{nH} or ω_{nL}. Taking into account ZVS characteristics of the inverter, ω_n is set to ω_{nH} [35]. According to (9) and (10) with ω_n=ω_{nH}, the voltage gain of the system, G_{vsys}, can be obtained with

$$G_{vsys}(\omega_n=\omega_{nH}, D_p)=G_{ivsys}\times R_L=\sqrt{\frac{L_2}{L_1}}\sin\left(\frac{D_p\pi}{2}\right) \tag{22}$$

In CV stage, the desired voltage gain of the system is defined as K_{cv} (=V_{2max}/V_1). By considering both the required K_{cv} and the minimum D_p, G_{vsys} should satisfy

$$\begin{cases} G_{vsys}(\omega_n=\omega_{nH}, D_p=1)\ge K_{cv} \\ G_{vsys}(\omega_n=\omega_{nH}, D_p=D_{pmin})\le K_{cv} \end{cases} \tag{23}$$

By substituting (22) into (23), the self-inductances of Tx and Rx coils in CV stage should satisfy

$$K_{cv}^2L_1\le L_2\le K_{cv}^2L_1\csc^2\left(\frac{D_{pmin}\pi}{2}\right) \tag{24}$$

Therefore, the range of L_2 in CV stage is independent of both k and R_L.

C. Boundary Constraints for Resonant Coil Currents

Since coil voltages depends on coil currents, once the maximum coil currents are determined, coil voltages can be easily calculated. Therefore, only the constraints on coil currents on both sides are considered here, which should be analyzed separately.

1) Constraints of Secondary Resonant Coil Current

As the secondary side adopts an uncontrolled rectifier, the secondary coil current I_{L2} is only related to the dc output current of the rectifier I_2 and is independent of the operating frequency of the inverter. Then, I_{L2} can be represented as

$$\begin{cases} I_{L2cc}=\dfrac{\pi}{2\sqrt{2}}\times I_{2max} & (a)\cdots\text{CC stage} \\ I_{L2cp}=\dfrac{\pi}{2\sqrt{2}}\times\sqrt{\dfrac{P_{2max}}{R_L}} & (b)\cdots\text{CP stage} \\ I_{L2cv}=\dfrac{\pi}{2\sqrt{2}}\times\dfrac{V_{2max}}{R_L} & (c)\cdots\text{CV stage} \end{cases} \tag{25}$$

In CC stage, I_{L2cc} is only dependent on I_{2max} and is independent of R_L. In CP stage, P_{2max} remains constant and I_{L2cp} decreases as R_L increases, reaching its maximum value when R_L=R_{LB}. In CV stage, V_{2max} remains constant and I_{L2cv} decreases as R_L increases, reaching its maximum value when R_L=R_{LC}.

In summary, during the whole charging process, it is only necessary to consider I_{L2cc} during CC stage to ensure that the maximum rms value of the secondary coil current does not exceed the preset value I_{L2safe}.

2) Constraints of Primary Resonant Coil Current

The constraints on the primary resonant coil current also needs to be discussed separately for each of three charging stages. According to Fig. 4(b), the primary coil current I_{L1} can be obtained with

$$I_{L1}(\omega_n)=\frac{I_{L2}\sqrt{64R_L^2\omega_n^2+\pi^4\omega_0^2L_2^2(\omega_n^2-1)^2}}{\pi^2k\sqrt{L_1L_2}\omega_0\omega_n^2} \tag{26}$$

Substituting (25).(a) into (26) with ω_n=1, the rms value of the primary coil current in CC stage can be derived as

$$I_{L1cc}=\frac{2\sqrt{2}I_{2max}R_L}{\pi k\omega_0\sqrt{L_1L_2}} \tag{27}$$

Based on (27), during CC stage, where I_{2max} remains constant, I_{L1cc} is a monotonically increasing function of R_L and a monotonically decreasing function of k. When R_L=R_{LB} and k=k_{min}, I_{L1cc} reaches its maximum. To ensure the safety of I_{L1cc} during CC stage, it should be ensured that its maximum rms value does not exceed the predetermined maximum rms value I_{L1safe} (i.e. $I_{L1cc}\leqslant I_{L1safe}$). Then, given that the range of k is [k_{min}, k_{max}] and the range of R_L is [R_{LA}, R_{LB}], the required self-

inductances L_1 and L_2 during CC stage should satisfy

$$L_2 \geq \frac{8I_{2\max}^2 R_{\mathrm{LB}}^2}{\pi^2 I_{\mathrm{L1safe}}^2 k_{\min}^2 \omega_0^2 L_1} \tag{28}$$

Substituting (25).(b) into (26) with ω_n=1, the rms value of the primary coil current in CP stage can be also be obtained. Similar to CC stage, to ensure the safety of I_{L1cp} during CP stage the required self-inductances L_1 and L_2 should satisfy

$$L_2 \geq \frac{8P_{2\max} R_{\mathrm{LC}}}{\pi^2 \omega_0^2 I_{\mathrm{L1safe}}^2 k_{\min}^2 L_1} \tag{29}$$

Based on the lower limit constraints for L_2 in CC and CP stages, by comparing (28) and (29), it can be inferred that

$$\frac{8P_{2\max} R_{\mathrm{LC}}}{\pi^2 \omega_0^2 I_{\mathrm{L1safe}}^2 k_{\min}^2 L_1} = \frac{8I_{2\max}^2 R_{\mathrm{LC}} R_{\mathrm{LB}}}{\pi^2 \omega_0^2 I_{\mathrm{L1safe}}^2 k_{\min}^2 L_1} > \frac{8I_{2\max}^2 R_{\mathrm{LB}}^2}{\pi^2 \omega_0^2 I_{\mathrm{L1safe}}^2 k_{\min}^2 L_1} \tag{30}$$

Therefore, according to (30), it's sufficient to focus solely on the lower limit of L_2 in CP stage. Substituting (25).(c) into (26) with ω_n=ω_{nH}, the rms value of the primary coil current in CV stage can be represented as

$$I_{\mathrm{L1cv}} = \frac{V_{2\max}}{2\sqrt{2}\pi\omega_0}\sqrt{\frac{64(1-k)}{L_1 L_2 k^2} + \frac{\pi^4 \omega_0^2 L_2}{R_{\mathrm{L}}^2 L_1}} \tag{31}$$

In CV stage, where $V_{2\max}$ remains constant, I_{L1cv} is a monotonically decreasing function of both R_{L} and k. Similarly, to ensure the safety of I_{L1cv} during CV stage, the required self-inductances L_1 and L_2 should satisfy

$$L_{2\mathrm{cvd}}^{(1)} \leq L_2 \leq L_{2\mathrm{cvu}}^{(1)} \tag{32}$$

where $L^{(1)}_{2\mathrm{cvd}}$ and $L^{(1)}_{2\mathrm{cvu}}$ represent:

$$\begin{cases} L_{2\mathrm{cvd}}^{(1)} = \dfrac{4I_{\mathrm{L1safe}}^2 L_1 R_{\mathrm{LC}}^2}{\pi^2 V_{2\max}^2} - \dfrac{4}{\pi^2}\sqrt{\dfrac{I_{\mathrm{L1safe}}^4 L_1^2 R_{\mathrm{LC}}^4}{V_{2\max}^4} - \dfrac{4\left(1-k_{\min}\right)R_{\mathrm{LC}}^2}{\omega_0^2 k_{\min}^2}} \\ L_{2\mathrm{cvu}}^{(1)} = \dfrac{4I_{\mathrm{L1safe}}^2 L_1 R_{\mathrm{LC}}^2}{\pi^2 V_{2\max}^2} + \dfrac{4}{\pi^2}\sqrt{\dfrac{I_{\mathrm{L1safe}}^4 L_1^2 R_{\mathrm{LC}}^4}{V_{2\max}^4} - \dfrac{4\left(1-k_{\min}\right)R_{\mathrm{LC}}^2}{\omega_0^2 k_{\min}^2}} \end{cases} \tag{33}$$

In order to ensure that (33) has the solution, the required primary self-inductance L_1 should satisfy:

$$L_1 \geq \frac{2V_{2\max}^2\sqrt{1-k_{\min}}}{\omega_0 k_{\min} I_{\mathrm{L1safe}}^2 R_{\mathrm{LC}}} \tag{34}$$

D. Boundary Conditions for Resonant Capacitor Voltages

Since capacitor currents depends on capacitor voltages, once the maximum capacitor voltages are determined, the capacitor currents can be easily obtained. Therefore, only the constraints on capacitor voltages are required to be considered here, which should also be analyzed separately.

1) Constraints of Secondary Resonant Capacitor Voltage

Based on (25), during three charging stages, the secondary resonant capacitor voltage V_{C2} can be obtained as

$$\begin{cases} V_{\mathrm{C2cc}} = \dfrac{\pi}{2\sqrt{2}} I_{2\max}\omega_0 L_2 & \text{(a)}\cdots\text{CC stage} \\ V_{\mathrm{C2cp}} = \dfrac{\pi}{2\sqrt{2}}\omega_0 L_2\sqrt{\dfrac{P_{2\max}}{R_{\mathrm{L}}}} & \text{(b)}\cdots\text{CP stage} \\ V_{\mathrm{C2cv}} = \dfrac{\pi}{2\sqrt{2}}\dfrac{V_{2\max}\omega_0 L_2\sqrt{1-k}}{R_{\mathrm{L}}} & \text{(c)}\cdots\text{CV stage} \end{cases} \tag{35}$$

Obviously, V_{C2cc} remains constant in CC stage. In addition, V_{C2cp} reaches its maximum values when R_{L}=R_{LB} in CP stage. At point B, V_{C2cc} equals V_{C2cp}. In CV stage, $V_{2\max}$ remains constant and V_{C2cv} decreases as R_{L} increases, reaching its maximum value when R_{L}=R_{LC}.

Based on (35), during three charging stages, it is required that the rms value of the secondary resonant capacitor voltage V_{C2} does not exceed the predetermined maximum rms value V_{C2safe}. By solving these inequalities, L_2 should satisfy

$$\begin{cases} 0 < L_2 \leq \dfrac{2\sqrt{2}V_{\mathrm{C2safe}}}{\pi\omega_0 I_{2\max}} = L_{2\mathrm{ua}} & \text{(a)}\cdots\text{CC stage} \\ 0 < L_2 \leq \dfrac{2\sqrt{2}V_{\mathrm{C2safe}}}{\pi\omega_0}\sqrt{\dfrac{R_{\mathrm{LB}}}{P_{2\max}}} = L_{2\mathrm{ub}} & \text{(b)}\cdots\text{CP stage} \\ 0 < L_2 \leq \dfrac{2\sqrt{2}R_{\mathrm{LC}}V_{\mathrm{C2safe}}}{\pi\omega_0 V_{2\max}\sqrt{1-k_{\min}}} = L_{2\mathrm{uc}} & \text{(c)}\cdots\text{CV stage} \end{cases} \tag{36}$$

According to (36).(a) and (b), in CC and CP stages, $L_{2\mathrm{ua}}$=$L_{2\mathrm{ub}}$. Therefore, the constraints of the upper boundaries of L_2 in CC and CP stage are equivalent. By comparing the constraints of the upper boundaries of L_2 in CP and CV stages with R_{LC}>R_{LB} and 0<$k_{\min}$<1, it can be obtained that

$$L_{2\mathrm{uc}} > \frac{2\sqrt{2}V_{\mathrm{C2safe}}}{\pi\omega_0}\sqrt{\frac{R_{\mathrm{LC}}}{P_{2\max}}} > \frac{2\sqrt{2}V_{\mathrm{C2safe}}}{\pi\omega_0}\sqrt{\frac{R_{\mathrm{LB}}}{P_{2\max}}} = L_{2\mathrm{ub}} \tag{37}$$

According to (37), it can be obtained that $L_{2\mathrm{uc}}$>$L_{2\mathrm{ua}}$=$L_{2\mathrm{ub}}$. Therefore, to ensure the safety of V_{C2cv} during CV stage, the secondary self-inductance L_2 should satisfy

$$0 \leq L_2 \leq \frac{2\sqrt{2}V_{\mathrm{C2safe}}}{\pi\omega_0}\sqrt{\frac{R_{\mathrm{LB}}}{P_{2\max}}} \tag{38}$$

2) Constraints of Primary Resonant Capacitor Voltage

Similarly, the constraints on the primary resonant capacitor voltage also needs to be discussed separately for each of three charging stages. According to (26), the primary resonant capacitor voltage V_{C1} can be obtained by

$$V_{\mathrm{C1}}(\omega_n) = \frac{I_{\mathrm{L2}} L_1\sqrt{64R_{\mathrm{L}}^2\omega_n^2 + \pi^4\omega_0^2 L_2^2(\omega_n^2-1)^2}}{\pi^2\omega_n^3 k\sqrt{L_1 L_2}} \tag{39}$$

In CC and CP stages, substituting (25).(a) and (b) into (39) and ω_n=1, respectively, V_{C1cc} and V_{C1cp} can be obtained by

$$\begin{cases} V_{\mathrm{C1cc}} = \dfrac{2\sqrt{2}I_{2\max}R_{\mathrm{L}}}{\pi k}\sqrt{\dfrac{L_1}{L_2}} & \text{(a)}\cdots\text{CC stage} \\ V_{\mathrm{C1cp}} = \dfrac{2\sqrt{2}}{\pi k}\sqrt{\dfrac{P_{2\max}R_{\mathrm{L}}L_1}{L_2}} & \text{(b)}\cdots\text{CP stage} \end{cases} \tag{40}$$

To ensure the safety of V_{C1cc} and V_{C1cp} during CC and CP stages, the secondary inductance L_2 should satisfy

$$\begin{cases} L_2 \geq \dfrac{8L_1 I_{2\max}^2 R_{\mathrm{LB}}^2}{\pi^2 V_{\mathrm{C1safe}}^2 k_{\min}^2} & \text{(a)}\cdots\text{CC stage} \\ L_2 \geq \dfrac{8L_1 P_{2\max} R_{\mathrm{LC}}}{\pi^2 V_{\mathrm{C1safe}}^2 k_{\min}^2} & \text{(b)}\cdots\text{CP stage} \end{cases} \tag{41}$$

By comparing the lower boundaries of L_2 in (41).(a) and (b), it can be obtained that

$$\frac{8L_1P_{2\max}R_{\mathrm{LC}}}{\pi^2V_{\mathrm{C1safe}}^2k_{\min}^2}=\frac{8L_1I_{2\max}^2R_{\mathrm{LB}}R_{\mathrm{LC}}}{\pi^2V_{\mathrm{C1safe}}^2k_{\min}^2}>\frac{8L_1I_{2\max}^2R_{\mathrm{LB}}^2}{\pi^2V_{\mathrm{C1safe}}^2k_{\min}^2} \tag{42}$$

Therefore, based on (42), it's sufficient to focus solely on the lower limit of L_2 in CP stage. Substituting (25).(c) into (39) and setting $\omega_{\mathrm{n}}=\omega_{\mathrm{nH}}$, during CV stage, V_{C1cv} can be derived as

$$V_{\mathrm{C1cv}}=\frac{V_{2\max}}{2\sqrt{2}\pi}\sqrt{\frac{64L_1}{L_2}\left(\frac{1}{k}-1\right)^2+\frac{\pi^4\omega_0^2L_1L_2\left(1-k\right)}{R_{\mathrm{L}}^2}} \tag{43}$$

As 0<k<1, based on (43), when $V_{2\max}$ remains constant, V_{C1cv} is a monotonically decreasing function of R_{L} and k. Hence, when $R_{\mathrm{L}}=R_{\mathrm{LC}}$ and $k=k_{\min}$, V_{C1cv} reaches its maximum value. To ensure the safe of V_{C1cv} during CV stage, the required self-inductances L_1 and L_2 should satisfy

$$L_{2\mathrm{cvd}}^{(2)}\le L_2\le L_{2\mathrm{cvu}}^{(2)} \tag{44}$$

where $L^{(2)}{}_{2\mathrm{cvu}}$ and $L^{(2)}{}_{2\mathrm{cvd}}$ represent:

$$\begin{cases}L_{2\mathrm{cvd}}^{(2)}=\dfrac{4R_{\mathrm{LC}}^2V_{\mathrm{C1safe}}^2}{\pi^2\omega_0^2\left(1-k_{\min}\right)V_{2\max}^2L_1}-\dfrac{4R_{\mathrm{LC}}\sqrt{\dfrac{k_{\min}^2R_{\mathrm{LC}}^2V_{\mathrm{C1safe}}^4}{L_1^2V_{2\max}^4}-4\omega_0^2\left(1-k_{\min}\right)^3}}{\pi^2\left(1-k_{\min}\right)k_{\min}\omega_0^2}\\ L_{2\mathrm{cvu}}^{(2)}=\dfrac{4R_{\mathrm{LC}}^2V_{\mathrm{C1safe}}^2}{\pi^2\omega_0^2\left(1-k_{\min}\right)V_{2\max}^2L_1}+\dfrac{4R_{\mathrm{LC}}\sqrt{\dfrac{k_{\min}^2R_{\mathrm{LC}}^2V_{\mathrm{C1safe}}^4}{L_1^2V_{2\max}^4}-4\omega_0^2\left(1-k_{\min}\right)^3}}{\pi^2\left(1-k_{\min}\right)k_{\min}\omega_0^2}\end{cases} \tag{45}$$

In order to ensure that (45) has the solution, the primary self-inductance L_1 should satisfy

$$L_1\le\frac{k_{\min}R_{\mathrm{LC}}V_{\mathrm{C1safe}}^2}{2V_{2\max}^2\omega_0\sqrt{\left(1-k_{\min}\right)^3}} \tag{46}$$

E. Summary of Multiple Boundary Constraints

By closely combining transfer characteristics of the resonant network, system control strategies, three-stage charging methods, variations of coupling coefficient, the voltage and current stresses on resonant components and the limitation of minimum phase-shift duty cycle, these upper and lower boundary values of self-inductances of Tx and Rx coils are listed and summarized in Table I. It is worth mentioning that the selected self-inductances of Tx and Rx coils must satisfy all boundary constraints to perform the optimal design of coils, which is named as MBCs.

IV. A Case-Study of Coil Design Based on MBCs

To provide a detailed introduction to the proposed universal resonant parameter design method of the WPT system based on MBCs in Fig. 3(b), a detailed explanation will be provided using a specific example in the following.

A. Example of Battery Fast Charging

Based on Fig. 3(b), the example of the battery fast charging by adopting three-stage charging stages will be given first. The

TABLE I
OPTIMIZED PARAMETER RANGES BASED ON MULTIPLE BOUNDARY CONSTRAINTS

Conditions	No.	Mode	Upper value of L_2	Low value of L_2	Condition
Output Requirements	1	CC	$\frac{64}{\pi^4\omega_0^2k_{\min}^2K_{\mathrm{cc}}^2L_1}\sin^2[\frac{D_{\mathrm{pmin}}\pi}{2}]$ *	$\frac{64}{\pi^4\omega_0^2k_{\max}^2K_{\mathrm{cc}}^2L_1}$ *	/
	2	CP	$\frac{64V_1^2R_{\mathrm{LC}}}{\pi^4\omega_0^2k_{\min}^2L_1P_{2\max}}\sin^2[\frac{D_{\mathrm{pmin}}\pi}{2}]$	$\frac{64V_1^2R_{\mathrm{LB}}}{\pi^4\omega_0^2k_{\max}^2L_1P_{2\max}}$	$\sin^2[\frac{D_{\mathrm{pmin}}\pi}{2}]<\frac{R_{\mathrm{LB}}k_{\min}^2}{R_{\mathrm{LC}}k_{\max}^2}$
	3	CV	$K_{\mathrm{cv}}^2L_1$	$K_{\mathrm{cv}}^2L_1\csc^2[\frac{D_{\mathrm{pmin}}\pi}{2}]$	/
I_{L1} limitations	4	CC	$\frac{8I_{2\max}^2R_{\mathrm{LB}}^2}{\pi^2\omega_0^2I_{\mathrm{L1safe}}^2k_{\min}^2L_1}$ *	/	/
	5	CP	$\frac{8P_{2\max}R_{\mathrm{LC}}}{\pi^2\omega_0^2I_{\mathrm{L1safe}}^2k_{\min}^2L_1}$	/	/
	6	CV	$L_{2\mathrm{cvd}}^{(1)}$ **	$L_{2\mathrm{cvu}}^{(1)}$ **	$L_1\ge\frac{2V_{2\max}^2\sqrt{1-k_{\min}}}{\omega_0k_{\min}I_{\mathrm{L1safe}}^2R_{\mathrm{LC}}}$
V_{C2} limitations	7	CC	/	$\frac{2\sqrt{2}V_{\mathrm{C2safe}}}{\pi\omega_0I_{2\max}}$ *	/
	8	CP	/	$\frac{2\sqrt{2}V_{\mathrm{C2safe}}}{\pi\omega_0}\sqrt{\frac{R_{\mathrm{LB}}}{P_{2\max}}}$	/
	9	CV	/	$\frac{2\sqrt{2}R_{\mathrm{LC}}V_{\mathrm{C2safe}}}{\pi\omega_0V_{2\max}\sqrt{1-k_{\min}}}$ *	/
V_{C1} limitations	10	CC	$\frac{8L_1I_{2\max}^2R_{\mathrm{LB}}^2}{\pi^2V_{\mathrm{C1safe}}^2k_{\min}^2}$ *	/	/
	11	CP	$\frac{8L_1P_{2\max}R_{\mathrm{LC}}}{\pi^2V_{\mathrm{C1safe}}^2k_{\min}^2}$	/	/
	12	CV	$L_{2\mathrm{cvd}}^{(2)}$ **	$L_{2\mathrm{cvu}}^{(2)}$ **	$L_1\le\frac{k_{\min}R_{\mathrm{LC}}V_{\mathrm{C1safe}}^2}{2V_{2\max}^2\omega_0\sqrt{(1-k_{\min})^3}}$

* Stands for redundant limitations. **The corresponding abbreviations are in the text (33) and (45).

TABLE II
BATTERY PARAMETERS WITH THE THREE-STAGE CHARGING

Name	Symbol	Value	Unit
Voltage range of the battery pack modules	V_2	64-144	V
Maximum charging current of the battery pack modules	I_{2max}	8	A
Maximum charging voltage of the battery pack modules	V_{2max}	144	V
Maximum charging power of the battery pack modules	P_{2max}	1000	W
Floating charge current of the battery pack modules	I_{2min}	2	A
Equivalent dc resistance of the battery packs at point A	R_{LA}	8	Ω
Equivalent dc resistance of the battery packs at point B	R_{LB}	15.63	Ω
Equivalent dc resistance of the battery packs at point C	R_{LC}	20.74	Ω
Equivalent dc resistance of the battery packs at point D	R_{LD}	72	Ω

target battery pack consists of 12 lead-acid battery modules connected in series, with the nominal capacity and voltage of individual battery modules being 40 A-h and 12 V, respectively. The specific battery parameters are listed in Table II.

B. Design Requirements

In Fig. 3(b), in addition to clarifying the battery parameters in Table II, before designing the resonant parameters, it is also necessary to determine the input dc voltage of the inverter, V_1, the resonant frequency of the resonant network, f_0, the minimum phase-shift duty cycle of the inverter, D_{pmin}, the range of the coupling coefficient, k, the maximum current rms values of Tx and Rx resonant coils for safe operation I_{L1safe} and I_{L2safe}, the maximum voltage rms values of Tx and Rx resonant capacitors for safe operation V_{C1safe} and V_{C2safe}. After determining these specific design specifications, based on Fig. 3(b), the most crucial step is to assume an appropriate maximum range for the coupling coefficient of Tx and Rx coils. The related design specifications are listed in Table III.

C. Optimized Selection Range of Resonant Parameters

Based on Table I, with the related parameters and specifications listed in Table II and Table III, the MBCs of self-inductances of Tx and Rx coils are calculated and plotted in Fig. 9(a). Line group ① represents the upper and lower limits of L_2 for satisfying output design requirements in CP stage (solid line for the upper limit and dashed line for the lower limit). Line group ② represents the upper and lower limits of L_2 for satisfying output design requirements in CV stage. Line ③ represents the lower limit of L_2 for safe operation of the primary coil in CP stage. Line ④ and ⑤ represent the limits of L_1 and L_2 for safe operation of the primary coil in CV stage. Line ⑥ represents the upper limit of L_2 for safe operation of the secondary resonant capacitor in CP stage. Line ⑦ represents the lower limit of L_2 for safe operation of the primary resonant capacitor in CP stage. Line ⑧ and ⑨ represent the limits of L_1 and L_2 for safe operation of the primary capacitor in CV stage. Considering all constraints, the optimized range of self-inductances of L_1 and L_2 will locate at the shaded yellow region in Fig. 9(a).

TABLE III
DESIGN SPECIFICATIONS OF INVERTER AND RESONANT NETWORK

Name	Symbol	Value	Unit
DC voltage of inverter	V_2	160	V
Minimum phase-shift duty cycle of inverter	D_{pmin}	0.265	/
Maximum rms value of primary resonant coil current	I_{L1safe}	16	A
Maximum rms value of secondary resonant coil current	I_{L2safe}	12	A
Maximum rms value of primary resonant capacitor voltage	V_{C1safe}	1000	V
Maximum rms value of secondary resonant capacitor voltage	V_{C2safe}	800	V
Maximum Range of coupling coefficient	k	0.15-0.20	/
Resonant frequency	f_0	85	kHz

It is worth mentioning that if the shaded region is non-existent or very small after plotting all boundary constraints, it indicates that the proposed design specifications are unreasonable and need to be re-optimized. Here, if the maximum rms value of primary resonant coil current I_{L1safe} is set as 12A and the other parameters in Table II and Table III remain unchanged, the MBCs of self-inductances of Tx and Rx

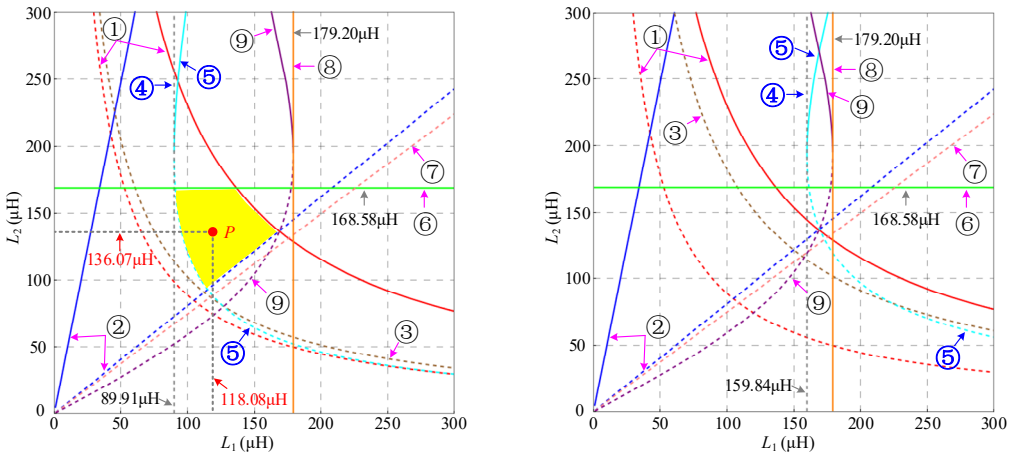

Fig. 9. MBCs of self-inductances of Tx and Rx coils with different I_{L1safe}. (a) MBCs with I_{L1safe}=16A. (b) MBCs with I_{L1safe}=12A.

TABLE IV
SPECIFIC STRUCTURAL PARAMETERS OF CIRCULAR COIL

Name	Symbol	Value	Unit
Radius of the starting point of the winding pad	R_S	50	mm
Radius of the ending point of the winding pad	R_E	230	mm
Winding pitch	δ	6	mm
Length of the winding pad	L_{pad}	500	mm
Width of the winding pad	W_{pad}	500	mm
Thickness of the winding pad	t_{pad}	15	mm
Length of the ferrite plate	L_F	450	mm
Width of the ferrite plate	W_F	450	mm
Thickness of the ferrite plate	t_F	5	mm
Distance between the winding and the ferrite plate	d_F	3.1	mm
Radius of the winding	r_0	2.1	mm

coils are calculated and plotted in Fig. 9(b). Obviously, in Fig. 9(b), there is no suitable shaded region that allows the WPT system to meet all the predefined specifications. Therefore, to achieve fast charging of the battery in Table II, the design specifications outlined in Table III need to be re-optimized to ensure the existence of a valid shaded range of self-inductances for Tx and Rx coils based on MBCs. Generally speaking, the MBCs-based design method of the WPT system not only considers multiple factors to enable the rational design of resonant network parameters but also assists engineers in optimizing design specifications, which significantly accelerates the design process and offers substantial practical value in engineering applications.

D. Coil Design Based on MBCs

Next, we will take the circular coil as an example to detail the MBCs-based design process of Tx and Rx coils.

1) Structure Parameters of a Single Coil

A single circular coil used in this article is shown in Fig. 10. The coil consists mainly of a coil winding and a ferrite plate, whose winding is a planar spiral extending from inside to outside. The radii of the starting and ending points of the coil winding are R_S and R_E, respectively. δ represents the winding pitch, which is the distance between the centers of two adjacent wires. r_0 is the radius of the wire. N_1 and N_2 represent the number of turns of Tx and Rx coils, respectively. W_F, L_F, and t_F represent the width, length, and thickness of the ferrite plate, respectively. d_F is the distance from the center of the wire to the top surface of the ferrite plate. The specific structural parameters are listed in Table IV.

2) Design of Coil Winding based on MBCs

Before designing the specific coils, it is necessary to determine the transfer distance and misalignment requirements of Tx and Rx coils, which are decided by practical applications. Table V provides an example of the transfer distance and misalignment requirements for the coil design.

After specifying the structural parameters of Tx and Rx coils in Table IV, the most critical step is to design the number of coil turns, which not only requires the self-inductances of Tx and Rx coils to fall within the shaded closed region in Fig. 9 based on MBCs, but also demands feasibility verification of

TABLE V
TRANSFER DISTANCE AND POSITIONAL MISALIGNMENT REQUIREMENTS

Name	Symbol	Value	Unit
Horizontal misalignment in X/Y direction	dx/dy	+/-50	mm
Horizontal misalignment in Z direction	dz	+/-10	mm
Standard vertical distance	H_{coil}	210	mm

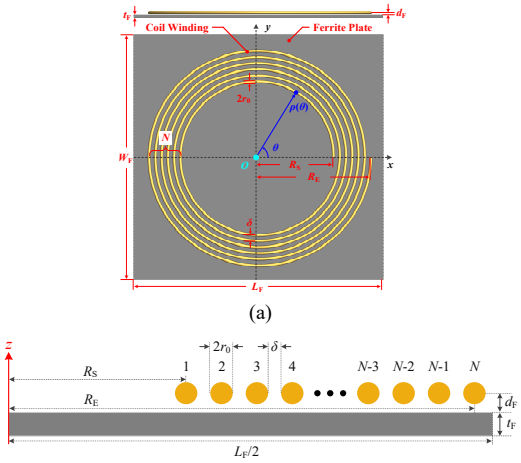

(a)

(b)

Fig. 10. Structure of the circular coil. (a) A top-down view of the circular coil. (b) Side view of the right half of the circular coil.

designed coils under the specific transfer distance and positional misalignments listed in Table V. To obtain better misalignment tolerances, the coils will be designed starting from the outermost turn of the winding pad when the winding pitch is fixed. With the aid of the Ansys Maxwell and the specific structural parameters listed in Table IV, the coil design results are that the number of turns for Tx and Rx coils are N_1=10 and N_2=11, respectively, with corresponding self-inductances of 118.08μH and 136.07μH, which is also plotted at point P in Fig. 9(a). The coupling coefficient of Tx and Rx coils obtained from simulation reaches its maximum and minimum values under No.1 and No.6 of Table VI, respectively, with values of 0.186 and 0.151. According to the proposed MBCs-based resonant parameter design method of the WPT system in Fig. 3(b), under the preset transfer distance and positional misalignments in Table V, the simulated coupling coefficient range of two coils falls precisely within the previously presumed range of 0.15–0.2. This indicates that the coil design result not only meets the transfer distance and positional misalignment requirements but also satisfies multiple design factors based on MBCs. Therefore, the coil design result represents an optimized and well-balanced solution with excellent overall performance.

V. EXPERIMENTAL EVALUATION

A. Experimental Prototype

1) Testing of Tx and Rx Circular Coils

Based on the previous analysis in Section IV.D, the designed circular coils with ferrite plates are shown in Fig. 11. They are tested by Impedance Analyzer (HIOKI IM3590) under different

misalignments. The experimental measurement results of Tx and Rx coils are shown in Table VI. The comparison results between the simulated results with Ansys Maxwell and the experimental results are plotted in Fig. 12. As shown in Fig. 12(a), the simulated and experimental results for the self-inductances of Tx and Rx coils match well, with a maximum error of less than 1μH between them. Meanwhile, Fig. 12(b) presents the simulated and experimental results for the mutual inductances of Tx and Rx coils also agree well under different misalignment conditions, with a maximum error of less than 1μH between them. The comparison results effectively demonstrate that the constructed coils fully meet the expected design results.

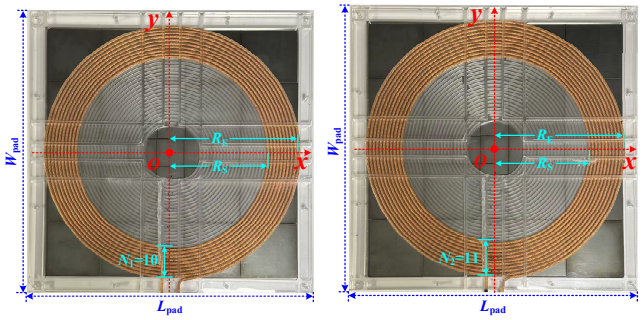

(a) (b)

Fig. 11. The designed winding pads of Tx and Rx circular coils. (a) N_1=10 for the primary circular coil. (b) N_2=11 for the secondary circular coil.

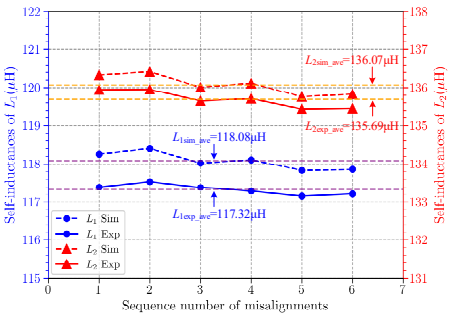

(a)

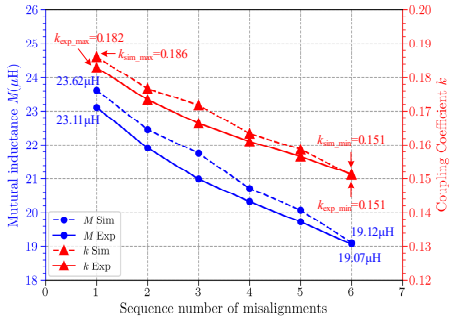

(b)

Fig. 12. Comparison of coil parameters between the simulated results and the measured ones. (a) Self-inductances of L_1 and L_2. (b) Mutual inductance and coupling coefficient of L_1 and L_2.

2) *Experimental Prototype of the WPT System*

To verify the previous analysis, a 1-kW experimental prototype is built up, which is shown in Fig. 13. The prototype includes a dc source (IT6536D), a high-frequency inverter, a SS resonant network, a full-bridge diode rectifier, and an electronic load (IT6006C). Electrical energy is transferred from the dc source to the electronic load. The primary inverter and secondary rectifier are controlled by two control boards based on DSP28377 respectively. The MOSFETs used in the inverter and the rectifier are IXTQ88N30Ps. The Tx and Rx controllers exchange information by the wireless communication modules (RF 2.4GHz). The coupled coils are made by the Litz wire that is composed of 1000 strands of fine wires, each with a diameter of 0.1 mm. The waveforms are recorded by the oscilloscope (LECROY HDO8058) and the overall system efficiency is measured by the power analyzer (WT5000). Detailed experimental parameters are listed in Table VII.

TABLE VI
EXPERIMENTAL MEASUREMENT RESULTS OF THE DESIGNED COILS

No.	dx (mm)	dz (mm)	L_1 (μH)	L_2 (μH)	M (μH)	k
1	0	-10	117.39	135.94	23.11	0.183
2	50	-10	117.53	135.95	21.91	0.173
3	0	0	117.38	135.65	20.99	0.166
4	50	0	117.28	135.71	20.32	0.161
5	0	10	117.15	135.44	19.73	0.157
6	50	10	117.21	135.46	19.07	0.151

TABLE VII
PARAMETERS OF THE WPT SYSTEM

Symbol	Quantity	Value
L_1	primary resonant inductor	117.32μH
C_1	primary resonant capacitor	29.88nF
f_1	primary resonant frequency	85kHz
R_1	primary ESR of resonant network	0.104Ω
L_2	secondary resonant inductor	135.69μH
C_2	secondary resonant capacitor	25.40nF
f_2	secondary resonant frequency	85.73kHz
R_2	secondary ESR of resonant network	0.119Ω
R_{dson}	on-time drain-to-source resistance of IXTQ88N30Ps	0.04Ω
R_L	load resistor	8-72Ω
d	face to face distance of coils	200-220mm
dx/dy	misalignment in the x/y direction	+/-50mm
k	coupling coefficient	0.183-0.151

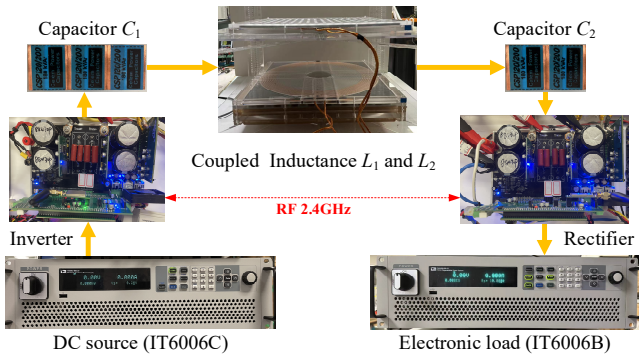

Fig. 13. Experimental prototype.

B. *Verification of Parameter Design with MBCs*

The coils designed with the MBCs-based design method require further validation and discussion regarding key design metrics and outcomes. These primarily include the resonant currents of Tx and Rx coils, the voltages of resonant capacitors on both sides, and the minimum phase-shift duty cycle of

inverter in the whole charging process. Here, the entire battery charging process is simulated by adjusting the load resistor R_L.

1) Verification of Minimum Phase-Shift Duty Cycle

Based on our previous analysis, a smaller phase-shift duty cycle D_p will not only results in higher switching losses of the inverter but also leads to greater THD. Therefore, it is essential to strictly limit the minimum value of D_p throughout the entire battery charging process. When R_L changes, Fig. 14 shows the comparisons between theoretical calculations and simulation measurements of D_p under different k during steady-state operation. The simulated D_p aligns well with the calculated one and the maximum difference between them is 8.24%, which validates the correctness of the theoretical derivation above.

In Fig. 14, during CC and CV stages, D_p remains almost constant regardless of variations of R_L. It is precisely because the control method and parameter design take into account the CC and CV characteristics of the resonant network that D_p remains almost unchanged with variations of R_L during CC and CV stages, which greatly reduces the difficulty of designing the closed-loop controller and enhances the stability of the WPT system. In CP stage, taking into account both coil misalignments and the minimum D_p restriction, the calculated D_p equals 0.367 with k=0.151, which fully meets the previous design requirements (D_{pmin}=0.265) in the charging process. This proves the effectiveness of the MBCs-based design method.

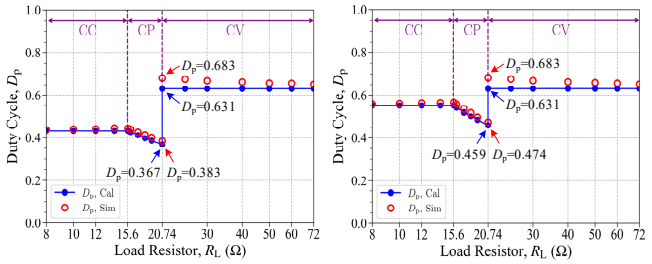

Fig. 14. Comparison of the calculated values with the simulated ones for D_p versus R_L in the three-stage charging process. (a) k=0.151. (b) k=0.183.

2) Verification of Resonant Coil Currents

By comparing the calculated results with the simulated results of I_{L1} and I_{L2} versus R_L in Fig. 15, the accuracy of the theoretical analysis can be validated. It can be obtained from Fig. 15 that in CC and CP stages of battery charging, I_{L1} will gradually increase as R_L increases. In CV stage, I_{L1} will decrease when R_L increases. When the CP stage turns into the CV stage, I_{L1} will increase suddenly due to the saltation of the inverter frequency. Obviously, when R_L=R_{LC} and ω_n=ω_{nH}, both the calculated results and simulated results of I_{L1} will reach their maximum values. Therefore, it is precisely due to the insertion of the CP charging stage that, while ensuring a 1kW charging power, the rms value of I_{L1} will be greatly reduced. This ensures the safe and stable operation of the WPT system without the need for overdesign.

In addition, during the charging process, I_{L2} will reach its maximum value in CC stage of battery charging, and then gradually decrease as R_L increases. The maximum values of the calculated results and simulated results of I_{L1} and I_{L2} are all below the preset maximum rms values of resonant currents of Tx and Rx coils, respectively, which proves the effectiveness of the MBCs-based design method.

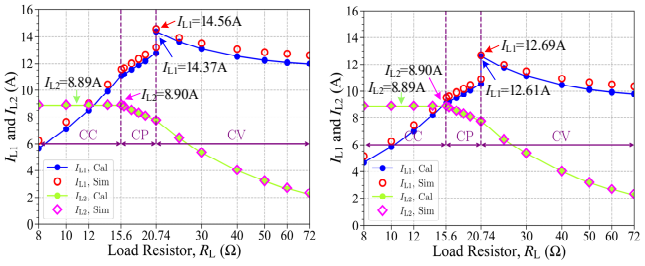

Fig. 15. Comparison of the calculated values with the simulated ones for I_{L1} and I_{L2} versus R_L in the three-stage charging process. (a) k=0.151. (b) k=0.183.

3) Verification of Resonant Capacitor Voltages

By comparing the calculated results with the simulated results of V_{C1} and V_{C2} versus R_L in Fig. 16, the accuracy of the theoretical analysis can also be validated. During the charging process, the variation trend of the resonant capacitor voltages is completely consistent with that of the resonant coil currents. It is worth mentioning that, due to the insertion of the CP charging stage, the rms value of V_{C1} is reduced, which eliminates the need for overdesign of the capacitor voltage. The maximum values of the calculated and simulated results of V_{C1} and V_{C2} are lower than the preset maximum values of resonant voltage V_{C1safe} for the primary capacitor and V_{C2safe} for the secondary capacitor, respectively, which also proves the effectiveness of the MBCs design method.

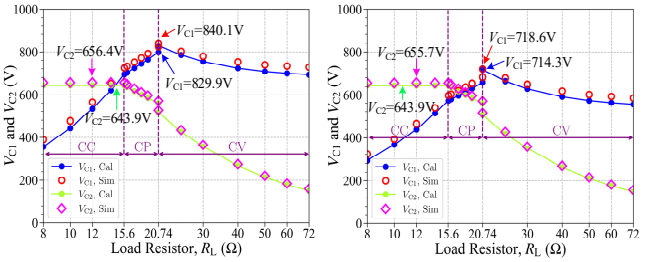

Fig. 16. Comparison of the calculated values with the simulated ones for V_{C1} and V_{C2} versus R_L in the three-stage charging process. (a) k=0.151. (b) k=0.183.

C. Performance Testing of the WPT System

In order to further verify the rationality of the coil design using the MBCs-based method, it is necessary to test the steady-state and dynamic performance of the WPT system throughout the entire charging process.

1) Testing of Steady-State Performance

The different charging stages of the battery are simulated by changing R_L. Fig. 17 presents the steady-state operating waveforms of the WPT system at different charging stages under the worst operating conditions (H_{coil} = 220mm and dx = 50mm). According to Fig. 17(a) and (b), when the WPT system operates in the CC and CP stages, the operating frequency is fixed at 85kHz, which enables the WPT system to achieve CC characteristics unaffected by load variations, contributing to improved system stability. In addition, during the CV stage, the operating frequency is switched from 85kHz to 92.25kHz,

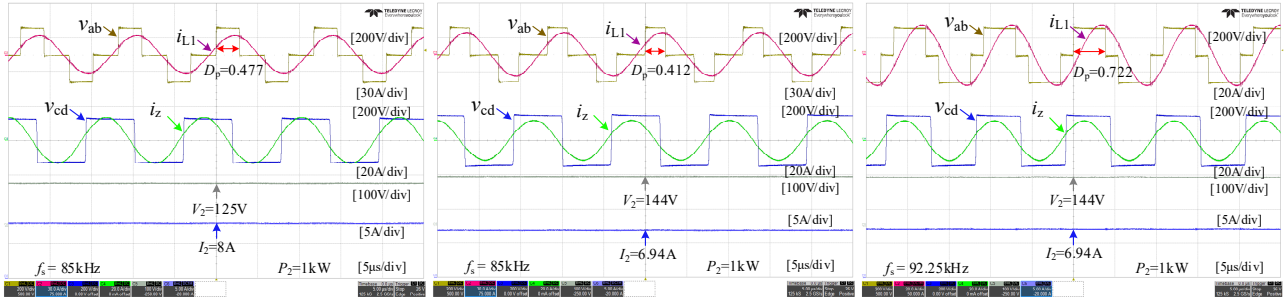

(a) (b) (c)

Fig. 17. Steady-state operating waveforms of the WPT system with the optimized coils under k=0.151 and V_1=160V. (a) In CC stage, I_2=8A and R_L=15.63Ω. (a) In CP stage, P_2=1kW and R_L=20.74Ω. (c) In CV stage, V_2=144V and R_L=20.74Ω.

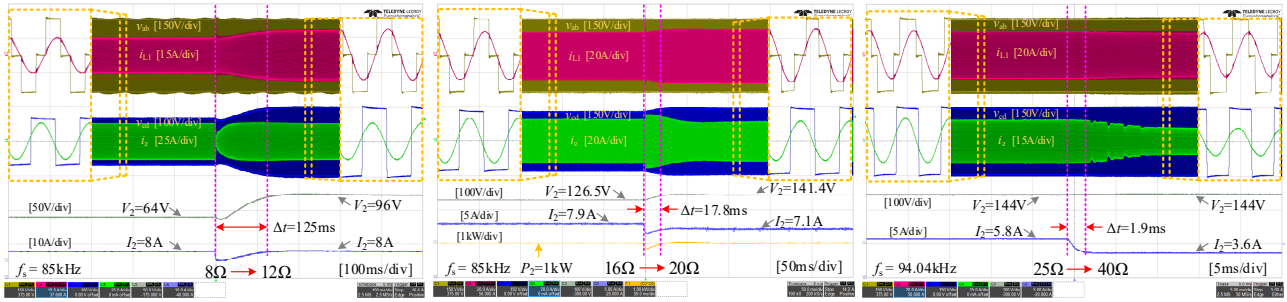

(a) (b) (c)

Fig. 18. Dynamic operating waveforms of the WPT system with the optimized coils under k=0.183 and V_1=160V. (a) In CC stage, I_2=8A and the step change of R_L from 8Ω to 12Ω. (a) In CP stage, P_2=1kW and the step change of R_L from 16Ω to 20Ω. (c) In CV stage, V_2=144V and the step change of R_L from 25Ω to 40Ω.

enabling the system to achieve CV characteristics unaffected by load variations under the worst operating conditions, which also contributes to improved system stability.

According to experimental results, throughout the full-range charging process of the battery, the predefined multiple design specifications, including phase-shift duty cycle, resonant coil currents, and resonant capacitor voltages, can all be satisfied under worst operating conditions. Therefore, it effectively demonstrates the validity of the proposed universal resonant parameter design method of the WPT system based on MBCs.

2) Testing of Dynamic Performance

As shown in Fig. 18, the dynamic performance of the WPT system against load disturbances at different charging stages is tested by introducing the step changes of the load resistor R_L.

Fig. 18(a) shows the dynamic responses of the WPT system in CC stage, where I_2 remains constant at 8A while R_L is abruptly changed from 8Ω to 12Ω. The dynamic setting time is 125ms. More effectively, Fig. 18(b) presents the dynamic responses of the WPT system in CP stage, where P_2 remains constant at 1kW while R_L is abruptly changed from 16Ω to 20 Ω. The dynamic setting time is 17.8ms. Even more surprisingly, Fig. 18(c) presents the dynamic responses of the WPT system in CV stage, where V_2 remains constant at 144V while R_L is abruptly changed from 25Ω to 40Ω. The dynamic setting time is only 1.9ms.

Although this paper does not model the entire control system or optimize the controller design, the WPT system still demonstrates excellent dynamic response and anti-disturbance performance, which is attributed to the careful consideration of its transfer characteristics when optimizing the design of the resonant network parameters. From this perspective, the coil optimization design method based on MBCs is also of significant importance for improving the system's dynamic response characteristics.

D. Comparison with Other Design Solutions

To further demonstrate the overall superior performance of our design, two other design results are selected as control groups for a comprehensive performance comparison. For a fair comparison, when selecting the coil design solutions for the control groups, we refer to the MBCs design results in Fig. 9(a) and choose two sets of coil design solutions that are close to the shaded region but not within it. The corresponding simulation models are then built in Fig. 19. Except for the difference in the number of coil turns, all other coil structural and positional parameters follow those listed in Table IV and Table V. The coil parameters and simulated results for these three cases are listed in Table VIII.

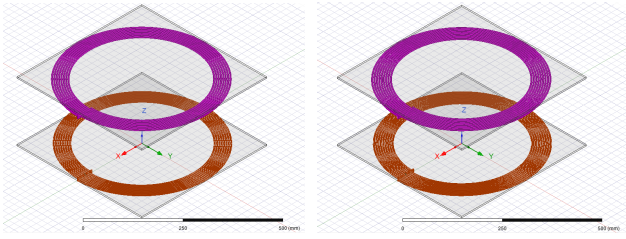

(a) (b)

Fig. 19. Two other design solutions for comparison with different number of coil turns for Tx and Rx coils. (a) Control Group A, N_1=N_2=8. (b) Control Group B, N_1=N_2=9.

These three solutions of coils are applied to implement the three-stage battery charging. Through MATLAB simulation, key design metrics are compared, including the resonant

TABLE VIII
COIL PARAMETERS FOR THREE CASES

Symbol	Control Group A (C. G. A)	Control Group B (C. G. B)	Optimal design in our paper
N_1	8	9	10
N_2	8	9	11
L_1 (μH)	83.69	100.60	118.08
L_2 (μH)	83.68	100.60	136.07
k_{min}	0.143	0.147	0.151
k_{max}	0.175	0.180	0.183

currents of Tx and Rx coils, the voltages of resonant capacitors on both sides, and the minimum phase-shift duty cycle of inverter in the whole charging process. As shown in Fig. 20, two radar charts are applied to compare the key design specifications of the WPT system under different coil positions with three different coil design solutions.

In Fig. 20, the regular pentagon formed by the orange dashed line represents the predefined design specifications of the WPT system in Table III. Since the phase-shift duty cycle D_p is expected to be greater than the preset D_{pmin} and a larger D_p actually corresponds to lower switching losses, the constraint on D_p is represented by the magnitude of the 1-D_p axis in the radar chart. Based on Fig. 20, it can be observed that only the optimal design in this study ensures that all key design indicators meet the predefined specifications in Table III. Compared with Control Group A and Control Group B, under the same transfer distance and misalignments while delivering the same power, despite the slight increase of V_{C2} caused by the tuning of the secondary resonant parameters, the optimal design in this study will exhibit lower I_{L1}, lower V_{C1}, larger D_p, lower inverter switching losses, and lower THD in the resonant network. This strongly demonstrates that the proposed universal resonant parameter design method of the WPT system based on MBCs can effectively provide an optimized and well-balanced solution for the WPT system with excellent overall performance.

E. System Transfer Efficiency

With the help of LFPSC strategy, the system charging power and transfer efficiency versus R_L under different misalignments are shown in Fig. 21. Here, the ever-changing R_L is applied to simulate the steady-state fast charging process.

In CC stage, as R_L gradually increases, the dc-dc transfer efficiency of the WPT system gradually increases. The exact opposite occurs in CP stage, where the transfer efficiency gradually decreases as R_L increases. In summary, during these two charging stages, the overall average transfer efficiency of the WPT system can achieve 92.53% at k=0.183 as well as 89.63% at k=0.151. However, when the WPT system switches from CP charging to CV charging, the dc-dc transfer efficiency of the system experiences a significant increase. This is because when the system operates at a high-frequency constant voltage gain point [ω_{nH} in Fig. 5.(b)], all switching devices of the inverter can achieve ZVS. Generally speaking, with a coupling coefficient k of 0.183 or 0.151, the maximum dc-dc system efficiency reaches 94.83% or 93.93%, respectively, under the rated-load condition (i.e., 1kW). Notably, when the WPT

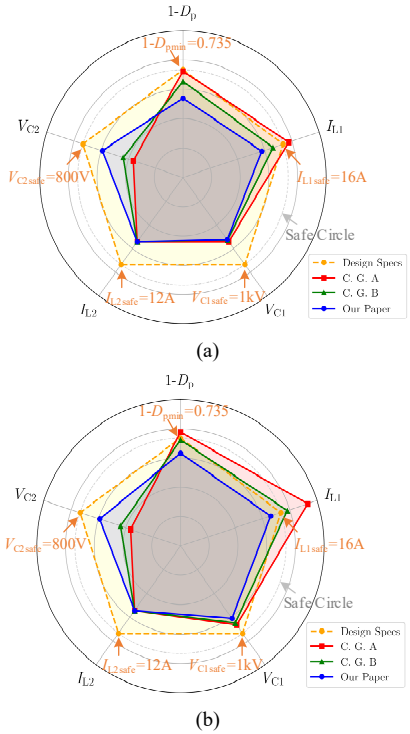

Fig. 20. Radar comparison charts of key design indicators for three different design solutions of Tx and Rx coils. (a) dx=dy=0mm and H_{coil} = 200mm. (b) dx=50mm, dy=0mm, and H_{coil} = 220mm.

system operates at point D (i.e. 28.8% of 1kW), the system efficiency remains as high as 91.25% or 87.87%, respectively.

Generally speaking, the experimental results demonstrate the well-designed WPT system with the universal resonant parameter design method based on MBCs not only achieve the multiple design targets mentioned before, but also achieve high transfer efficiency throughout the full range of battery charging. Therefore, the MBCs-based design method of the WPT system exhibits an optimized and well-balanced solution with excellent overall performance, which is of great significance for practical engineering applications.

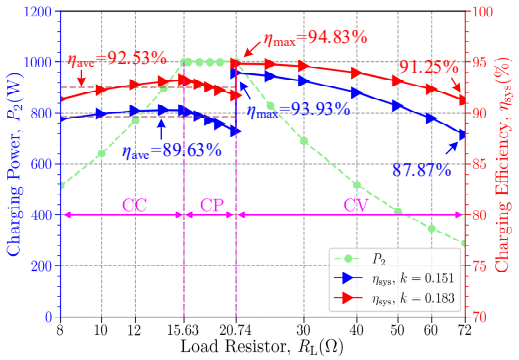

Fig. 21. Charging power and charging efficiency in three-stage charging process.

VI. CONCLUSION

This article takes the SS-type WPT system for fast battery charging as an example and proposes a universal resonant parameter design method of the WPT system based on MBCs.

This method innovatively transforms all design considerations into constraint relationships and utilizes a two-dimensional plane graph to optimize self-inductances of Tx and Rx coils. The proposed MBCs-based parameter design method not only exhibits the optimal design of self-inductances for Tx and Rx coils but also assists designers in revising unreasonable design indicators, significantly boosting design efficiency and ensuring the design results completely leverage superior system performance. Experimental results demonstrate that the resonant coils with the MBCs-based design method enable the WPT system to meet all predefined specifications while achieving steady-state and dynamic performance, accompanied by satisfactory dc-dc charging efficiency. Therefore, this design method allows the designed WPT system to achieve fast, stable, and safe battery charging at lower costs and higher charging efficiency, which is crucial for practical applications.

VII. REFERENCES

[1] S. Roy, A. N. M. W. Azad, S. Baidya, M. K. Alam, and F. Khan, "Powering Solutions for Biomedical Sensors and Implants Inside the Human Body: A Comprehensive Review on Energy Harvesting Units, Energy Storage, and Wireless Power Transfer Techniques," *IEEE Trans. Power Electron.*, vol. 37, no. 10, pp. 12237-12263. 2022.

[2] R. Sedehi *et al.*, "A Wireless Power Method for Deeply Implanted Biomedical Devices via Capacitively Coupled Conductive Power Transfer," *IEEE Trans. Power Electron.*, vol. 36, no. 2, pp. 1870-1882, 2021/1/1. 2021.

[3] A. D. de Sousa, L. F. M. Vieira, and M. A. M. Vieira, "Optimal Transmission Range and Charging Time for Qi-Compliant Systems," *IEEE Trans. Power Electron.*, vol. 35, no. 12, pp. 12765-12772. 2020.

[4] J. Zhu, Y. Ban, R. Xu, and C. C. Mi, "An NFC-Connected Coupler Using IPT-CPT-Combined Wireless Charging for Metal-Cover Smartphone Applications," *IEEE Trans. Power Electron.*, vol. 36, no. 6, pp. 6323-6338. 2021.

[5] L. M. *et al.*, "UAV Fleet Charging on Telecom Towers With Differential Capacitive Wireless Power Transfer," *IEEE Trans. Power Electron.*, pp. 1-16, 2024/1/1. 2024.

[6] D. Wang, F. Chen, J. Zhang, S. Cui, Z. Bie, and C. Zhu, "A Novel Pendulum-Type Magnetic Coupler With High Misalignment Tolerance for AUV Underwater Wireless Power Transfer Systems," *IEEE Trans. Power Electron.*, vol. 38, no. 12, pp. 14861-14871, 2023/1/1. 2023.

[7] K. Zhang, Y. Ma, Z. Yan, Z. Di, B. Song, and A. P. Hu, "Eddy Current Loss and Detuning Effect of Seawater on Wireless Power Transfer," *IEEE J. Emerg. Sel. Top. Power Electron.*, vol. 8, no. 1, pp. 909-917. 2020.

[8] L. J. Chen, J. T. Boys, and G. A. Covic, "Power Management for Multiple-Pickup IPT Systems in Materials Handling Applications," *IEEE J. Emerg. Sel. Top. Power Electron.*, vol. 3, no. 1, pp. 163-176. 2015.

[9] C. Jiang, K. T. Chau, C. Liu, and W. Han, "Design and Analysis of Wireless Switched Reluctance Motor Drives," *IEEE Trans. Ind. Electron.*, vol. 66, no. 1, pp. 245-254. 2019.

[10] Y. Li, S. Wang, Y. Wu, Y. Jiang, Z. Xiao, and Y. Tang, "Heterogeneous Integration of Isotropic and Anisotropic Magnetic Cores for Inductive Power Transfer," *IEEE Trans. Power Electron.*, pp. 1-15. 2024.

[11] M. Wu *et al.*, "A Compact Coupler With Integrated Multiple Decoupled Coils for Wireless Power Transfer System and its Anti-Misalignment Control," *IEEE Trans. Power Electron.*, vol. 37, no. 10, pp. 12814-12827. 2022.

[12] M. Wu *et al.*, "A Dual-Sided Control Strategy Based on Mode Switching for Efficiency Optimization in Wireless Power Transfer System," *IEEE Trans. Power Electron.*, vol. 36, no. 8, pp. 8835-8848. 2021.

[13] I. Tesla. "We, Robot." Available: https://www.tesla.com/we-robot, 2024.

[14] Y. Wu, Y. Jiang, Y. Li, H. Yuan, X. Wang, and Y. Tang, "Precise Parameterized Modeling of Coil Inductance in Wireless Power Transfer Systems," *IEEE Trans. Power Electron.*, vol. 39, no. 9, pp. 11746-11757. 2024.

[15] G. Buja, M. Bertoluzzo, and K. N. Mude, "Design and Experimentation of WPT Charger for Electric City Car," *IEEE Trans. Ind. Electron.*, vol. 62, no. 12, pp. 7436-7447. 2015.

[16] M. Kim, H. Park, and J. Jung, "Practical Design Methodology of IH and IPT Dual-Functional Apparatus," *IEEE Trans. Power Electron.*, vol. 35, no. 9, pp. 8897-8901, 2020/1/1. 2020.

[17] Z. Luo, X. Wei, M. G. S. Pearce, and G. A. Covic, "Multiobjective Optimization of Inductive Power Transfer Double-D Pads for Electric Vehicles," *IEEE Trans. Power Electron.*, vol. 36, no. 5, pp. 5135-5146. 2021.

[18] Wireless Power Transfer for Light-Duty Plug-In/Electric Vehicle and Alignment Methodology,", 2019.

[19] Z. Huang, T. Qin, X. L. Li, L. Ding, H. H. Iu, and C. K. Tse, "Synthesis of Inductive Power Transfer Converters with Dual Immittance Networks for Inherent CC-to-CV Charging Profiles," *IEEE Trans. Power Electron.*, vol. 39, no. 6, pp. 1-12, 2024/1/1. 2024.

[20] Z. Li, J. He, Y. Huo, M. Ban, Y. Liu, and J. Liu, "High-Misalignment Tolerance and Output Adjustable Wireless Charging System Via Detuned Series-Series Compensated Reconfigurable Transmission Channels," *IEEE Trans. Power Electron.*, vol. 38, no. 10, pp. 1-15, 2023/1/1. 2023.

[21] K. Song, Z. Li, J. Jiang, and C. Zhu, "Constant Current/Voltage Charging Operation for Series-Series and Series-Parallel Compensated Wireless Power Transfer Systems Employing Primary-Side Controller," *IEEE Trans. Power Electron.*, p. 1. 2018.

[22] Y. Jiang, L. Wang, J. Fang, R. Li, R. Han, and Y. Wang, "A High-Efficiency ZVS Wireless Power Transfer System for Electric Vehicle Charging WithVariable Angle Phase Shift Control," *IEEE J. Emerg. Sel. Top. Power Electron.*, vol. 9, no. 2, pp. 2356-2372, 2021/1/1. 2021.

[23] K. Liu, K. Li, Q. Peng, and C. Zhang, "A brief review on key technologies in the battery management system of electric vehicles," *Front. Mech. Eng.*, vol. 14, no. 1, pp. 47-64. 2019.

[24] M. Yilmaz and P. T. Krein, "Review of Battery Charger Topologies, Charging Power Levels, and Infrastructure for Plug-In Electric and Hybrid Vehicles," *IEEE Trans. Power Electron.*, vol. 28, no. 5, pp. 2151-2169. 2013.

[25] I. Iam, C. Choi, C. Lam, P. Mak, and R. P. Martins, "A Constant-Power and Optimal-Transfer-Efficiency Wireless Inductive Power Transfer Converter for Battery Charger," *IEEE transactions on industrial electronics (1982)*, vol. 71, no. 1, pp. 450-461, 2024/1/1. 2024.

[26] M. Budhia, G. A. Covic, and J. T. Boys, "Design and Optimization of Circular Magnetic Structures for Lumped Inductive Power Transfer Systems," *IEEE Trans. Power Electron.*, vol. 26, no. 11, pp. 3096-3108. 2011.

[27] Z. Huang, S. Wong, and C. K. Tse, "Design of a Single-Stage Inductive-Power-Transfer Converter for Efficient EV Battery Charging," *IEEE Trans. Veh. Technol.*, vol. 66, no. 7, pp. 5808-5821. 2017.

[28] R. Bosshard, J. W. Kolar, J. Muhlethaler, I. Stevanovic, B. Wunsch, and F. Canales, "Modeling and η - α -Pareto Optimization of Inductive Power Transfer Coils for Electric Vehicles," *IEEE J. Emerg. Sel. Top. Power Electron.*, vol. 3, no. 1, pp. 50-64. 2015.

[29] M. M., A. A., M. A., and S. A., "Pareto optimization of circular power pads for contactless electric vehicle battery charger," *2016 IEEE Industry Applications Society Annual Meeting*, 2016, pp. 1-6.

[30] H. Li, J. Li, K. Wang, W. Chen, and X. Yang, "A Maximum Efficiency Point Tracking Control Scheme for Wireless Power Transfer Systems Using Magnetic Resonant Coupling," *IEEE Trans. Power Electron.*, vol. 30, no. 7, pp. 3998-4008. 2015.

[31] Q. Chen, S. C. Wong, C. K. Tse, and X. Ruan, "Analysis, Design, and Control of a Transcutaneous Power Regulator for Artificial Hearts," *IEEE Trans. Biomed. Circuits Syst.*, vol. 3, no. 1, pp. 23-31. 2009.

[32] W. Zhang, S. Wong, C. K. Tse, and Q. Chen, "Design for Efficiency Optimization and Voltage Controllability of Series – Series Compensated Inductive Power Transfer Systems," *IEEE Trans. Power Electron.*, vol. 29, no. 1, pp. 191-200. 2014.

[33] L. Jiang and D. Costinett, "A High-Efficiency GaN-Based Single-Stage 6.78 MHz Transmitter for Wireless Power Transfer Applications," *IEEE Trans. Power Electron.*, vol. 34, no. 8, pp. 7677-7692. 2019.

[34] Y. Jiang, L. Wang, J. Fang, C. Zhao, K. Wang, and Y. Wang, "A Joint Control With Variable ZVS Angles for Dynamic Efficiency Optimization in Wireless Power Transfer System," *IEEE Trans. Power Electron.*, vol. 35, no. 10, pp. 11064-11081, 2020/1/1. 2020.

[35] Y. Jiang, L. Wang, Y. Wang, J. Liu, X. Li, and G. Ning, "Analysis, Design, and Implementation of Accurate ZVS Angle Control for EV Battery Charging in Wireless High-Power Transfer," *IEEE Trans. Ind. Electron.*, vol. 66, no. 5, pp. 4075-4085, 2019/1/1. 2019.